Full field measurements of curvature using coherent gradient sensing: application to thin film characterization

A.J. Rosakis[a], R.P. Singh[a,*], Y. Tsuji[b], E. Kolawa[b,c], N.R. Moore Jr.[c]

[a]*Department of Aeronautics, California Institute of Technology, Pasadena, CA 91125, USA*
[b]*Department of Applied Physics, California Institute of Technology, Pasadena, CA 91125, USA*
[c]*Jet Propulsion Laboratory, Pasadena, CA 91109,USA*

Abstract

This paper introduces coherent gradient sensing (CGS) as an optical, full-field, real-time, non-intrusive and non-contact technique for measurement of curvature and curvature changes in thin film and micro-mechanical structures. The technique is applied to determine components of the curvature tensor field in multilayered thin films deposited on silicon wafers. Curvature field measurements using CGS are compared with average curvatures obtained using high-resolution X-ray diffraction. Finally, examples are presented to demonstrate the capability of CGS in measuring curvature in a variety of thin film and micro-mechanical structures. © 1998 Elsevier Science S.A. All rights reserved

Keywords: Stress; Surface defects; Surface morphology; X-ray diffraction

1. Introduction

As the electronics industry pushes for smaller and smaller dimensions of metal interconnections and for more complex multilayered structures, the mechanical properties and stresses of thin films used for these interconnections becomes crucial to the lifetimes of ultra large scale integrated circuits [1,2]. However, the difficulty in measuring the mechanical properties and stresses of interconnections increases as their size decreases [3]. Currently, the major concern for the interconnection materials is residual stresses present in these materials as a result of the fabrication process and additional stresses resulting from thermal cycling [4–6].

Typically, integrated circuit metallization consists of many layers deposited onto a silicon substrate, very often at elevated temperatures. The layers exhibit different mechanical, physical and thermal properties leading to high stresses in interconnection structures. These stresses cause stress induced voiding [7–21], are directly related

to electromigration [22–29] and may cause cracking of the substrate [3]. All of which are leading failure mechanisms in integrated circuits. An understanding of stresses, their distribution, and origins is a crucial step in improving reliability of integrated circuits.

Currently used experimental techniques for measuring stresses are based either on direct measurements of strains in the films using X-ray diffraction [30,31] or on the measurements of substrate curvature or deflection [32]. Curvature and curvature change measurements are typically related to the stress state in the layered structures by means of theoretical analyses based either on approximate plate theories [33,34] or more recently on exact continuum mechanics formulation [35,36].

The X-ray diffraction technique typically employed for polycrystalline materials involves measuring d-spacings of a single reflection for several orientations of the sample [30]. This determines strains along different directions of the sample. The technique is non-destructive, does not require special sample configurations and it permits a measurements of all the components of stress in the film. However, it is limited to crystalline materials, e.g. stresses in passivation layers cannot be measured, and is difficult to

* Corresponding author. Tel.: +1 818 3954527; fax: +1 818 4492677; e-mail: raman@atlantis.caltech.edu

use in-situ during film growth. Moreover, the method is strictly point-wise, i.e. full-field, instantaneous measurement of stresses is not possible.

Curvature measurements in thin films can be made by high-resolution X-ray diffraction using a modified X-ray rocking curve setup [31]. With a translation stage added to the conventional rocking curve system, the shift in the substrate Bragg peak can be measured at different lateral positions on a film deposited on a single-crystal substrate. The average principal stresses can then be found from the peak shift. The primary limitation of this technique is that it requires calibration and curvatures are measured only relative to the reference calibration specimen. Also, the technique cannot be easily adapted for in-situ measurements since motion of the sample is required. In addition, since the method is strictly point-wise, full-field, instantaneous curvature measurements are not possible. Finally, in order to obtain good angular sensitivity for the peak shifts, the sample stage should be capable of translation of several millimeters with rotation less than 10^{-4} degrees.

Laser scanning is the most commonly used technique for measuring stresses in thin films by measuring curvature changes of the substrate [32]. This technique is very sensitive and it is capable of detecting up to 10^4 m radius of curvature. However, the laser scanning technique provides point-wise information and could potentially miss localized anomalies in specimen curvature. Even if complete curvature maps were generated by scanning, these scans would involve finite time and may not be adequate for time varying, non-uniform surface curvature fields (e.g. a growing delamination due to thermal cycling).

Techniques based on optical interferometry offer much promise as a means for real-time, remote, non-intrusive, full-field measurements of curvature and curvature changes. However, standard interferometric techniques, such as Twyman–Green interferometry [37–39], are sensitive to rigid body rotation and displacement of the specimen surface and thus are very vibration sensitive. Moreover, since these interferometric techniques measure the surface topography two successive differentiations of the experimental data are required to obtain curvature.

In this paper, we introduce coherent gradient sensing (CGS) as a full-field, optical technique for the instantaneous measurement of curvature and curvature changes. Comparison is made with curvatures measured using high-resolution X-ray diffraction.

2. Curvature measurement using CGS in reflection

Fig. 1 shows a schematic of the CGS setup in reflection. A coherent, collimated laser beam is directed to the specularly reflecting specimen surface by means of a beam splitter. The reflected beam from the specimen then passes through the beam splitter and is then incident upon a pair of identical high-density (40 lines/mm) Ronchi gratings, G_1 and G_2, separated by a distance Δ. The diffracted orders from the two grating are spatially filtered using a filtering lens to form distinct diffraction spots on the filter plane. An aperture placed in this plane serves to filter out the diffraction order of interest, which is then imaged onto the film plane. For our purpose, either of the ± 1 diffraction orders is of interest, as will become clear in the following discussion.

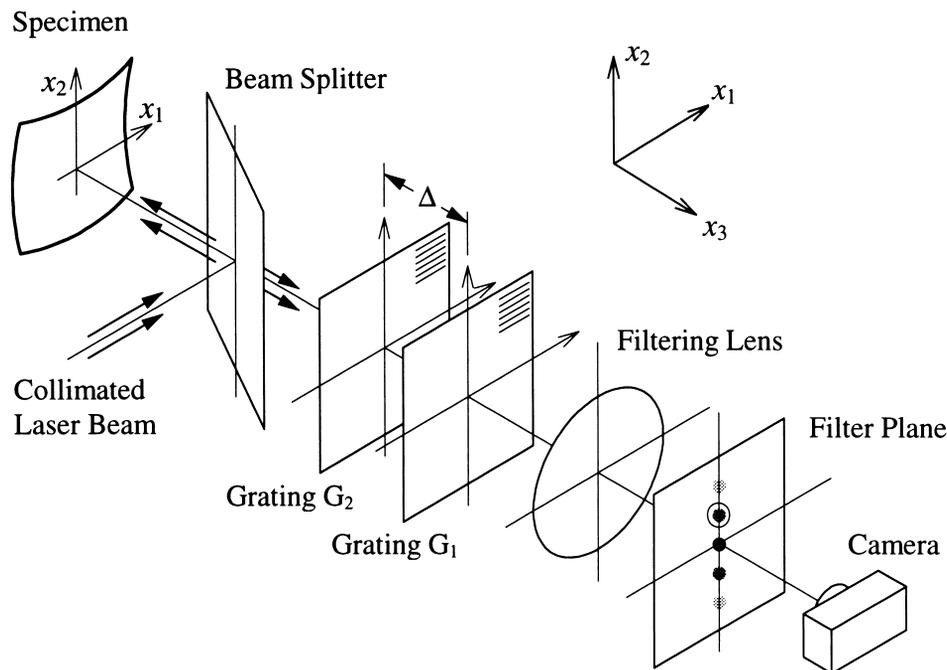Fig. 2 illustrates the working principle of CGS in two

Fig. 1. Schematic of the CGS setup in reflection mode.

dimensions. Consider an optical wave front incident on the grating pair and let both the gratings have their rulings along the x_2 axis. A wave front incident on the primary grating, G_1, is diffracted into several wave fronts denoted as E_0, E_1, E_{-1}, E_2, E_{-2}, etc. For illustrative purposes, only E_0, E_1, and E_{-1} are shown in Fig. 2. Each of these wave fronts are further diffracted by the second grating, G_2, to give rise to wave fronts denoted as $E_{0,0}$, $E_{0,1}$, $E_{0,-1}$..., $E_{1,0}$, $E_{1,1}$, $E_{1,-1}$..., $E_{-1,0}$, $E_{-1,1}$, $E_{-1,-1}$, etc. Again, only some of the diffracted wave fronts are shown. Now, various sets of parallel diffracted beams are combined using the filtering lens to form diffraction spots D_{+1}, D_0, D_{-1},... in the filter plane (which coincides with the focal plane of the lens). For example, $E_{0,1}$ and $E_{1,0}$ interfere to give diffraction spot D_{+1}, $E_{1,-1}$, $E_{0,0}$ and $E_{-1,1}$ interfere to give D_0, etc. An aperture is placed on the filter plane to block all but the D_{+1} diffraction spot. Subsequently, this diffraction spot is imaged onto the film plane.

Assume that the optical wave front incident on the first grating, G_1, is approximately planar and has a local phase difference given as $S(x_1, x_2)$. The net effect of the two gratings is to produce a lateral shift, or 'shearing', of the incident wave front. Thus, the optical wave front along the diffracted beam $E_{1,0}$ (given by $S(x_1, x_2 + \omega)$) is shifted by an amount ω along the x_2-direction as compared to the wave front along the diffracted beam $E_{0,1}$ (given by $S(x_1, x_2)$). The wave front shift is parallel to the principal axis of the gratings, i.e. along x_2 if the grating lines are oriented along x_1 as shown in Fig. 2. Moreover, the magnitude of the shift is a function of the grating separation, Δ, and the diffraction angle, θ, as

$$\omega = \Delta \tan\theta \tag{1}$$

where the diffraction angle, θ, is given by

$$\theta = \arcsin\lambda / p \tag{2}$$

with λ being the wavelength of light and p being the grating pitch. For a small angle of diffraction Eqs. (1) and (2) approximate to

$$\omega \approx \Delta\theta \tag{3}$$

$$\theta \approx \frac{\lambda}{p} \tag{4}$$

Now, consider the interference of the original and shifted wave fronts. The conditions for constructive interference may be expressed as

$$S(x_1, x_2 + \omega) - S(x_1, x_2) = n^{(2)}\lambda, \quad n^{(2)} = 0, \pm 1, \pm 2, \ldots \tag{5}$$

where, $n^{(2)}$ represents the integer identifying fringes observed for shearing along the x_2-direction.

Dividing Eq. (5) by ω gives

$$\frac{S(x_1, x_2 + \omega) - S(x_1, x_2)}{\omega} = \frac{n^{(2)}\lambda}{\omega}, \quad n^{(2)} = 0, \pm 1, \pm 2, \ldots \tag{6}$$

which, for sufficiently small ω, may be approximated by

$$\frac{\partial S(x_1, x_2)}{\partial x_2} = \frac{n^{(2)}\lambda}{\omega}, \quad n^{(2)} = 0, \pm 1, \pm 2, \ldots \tag{7}$$

Using Eqs. (3) and (4) in Eq. (7), we have

$$\frac{\partial S(x_1, x_2)}{\partial x_2} = \frac{n^{(2)}p}{\Delta}, \quad n^{(2)} = 0, \pm 1, \pm 2, \ldots \tag{8}$$

Generalizing the result to include wave front 'shearing' in either the x_1- or the x_2-direction, we have

$$\frac{\partial S(x_1, x_2)}{\partial x_2} = \frac{n^{(\alpha)}p}{\Delta}, \quad n^{(\alpha)} = 0, \pm 1, \pm 2, \ldots \tag{9}$$

where $n^{(\alpha)}$ represents the fringes observed for shearing along the x_α-direction and $\alpha \in \{1, 2\}$. Eq. (9) are the governing equation for interferograms formed using the technique of CGS. A substantially more involved derivation of Eq. (3) has been determined by using Fourier optics [40]. However, the above simple demonstration of the physical principle of CGS suffices for the purposes of this paper.

For a curved surface, the optical wave front may be interpreted in terms of the topography of the surface as follows.
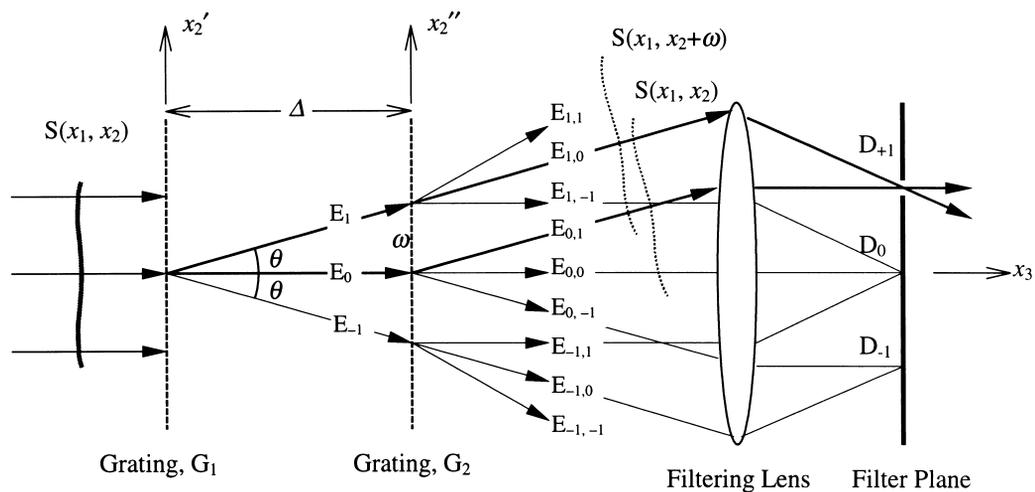

Fig. 2. Schematic to illustrate the working principle of CGS.

Consider a specularly reflective specimen whose curved surface (i.e. the reflector) can be expressed as

$$F(x_1, x_2, x_3) = x_3 - f(x_1, x_2) = 0 \tag{10}$$

The unit surface normal N at a generic point (x_1, x_2) of this curved surface is given by (see Fig. 3)

$$N = \frac{\nabla F}{|\nabla F|} = \frac{-f_{,1}\mathbf{e}_1 - f_{,2}\mathbf{e}_2 + \mathbf{e}_3}{\sqrt{1 + f_{,1}^2 + f_{,2}^2}} \tag{11}$$

where $f_{,\alpha}$ denotes in-plane gradient components of the specimen surface $x_3 = f(x_1, x_2)$, $(\alpha \in \{1, 2\})$, and $\mathbf{e}_i$ is the unit vector along the x_i axis, $(i = 1, 2, 3)$. Now, consider an initially planar wave front incident on the specimen surface, such that incident wave front is parallel to the (x_1, x_2) plane. The unit incident wave propagation vector (vector normal to the incident wave front) is given as

$$\mathbf{d}_0 = -\mathbf{e}_3 \tag{12}$$

If the specimen surface was flat and occupied the (x_1, x_2) plane the unit reflected wave propagation vector (vector normal to the reflected wave front) would be collinear with the incident vector and would be given as

$$\mathbf{d} = \mathbf{e}_3 \tag{13}$$

However, since the specimen surface is curved the reflected wave front is perturbed and the unit reflection propagation vector can be expressed as

$$\mathbf{d} = \alpha\mathbf{e}_1 + \beta\mathbf{e}_2 + \gamma\mathbf{e}_3 \tag{14}$$

where $\alpha(x_1, x_2)$, $\beta(x_1, x_2)$ and $\gamma(x_1, x_2)$ denote the direction cosines of the reflected (perturbed) wave front. From the law of reflection the unit incident wave propagation vector, $\mathbf{d}_0$, the unit reflected wave propagation vector, $\mathbf{d}$, and the unit surface normal, $\mathbf{N}$, are coplanar and related by (see Fig. 3)

$$\mathbf{d} \cdot \mathbf{N} = (-\mathbf{d}_0)\mathbf{N} = \mathbf{e}_3 \cdot \mathbf{N} \tag{15}$$

This leads to the relation

$$\mathbf{d} = (2\mathbf{e}_3 \cdot \mathbf{N})\mathbf{N} - \mathbf{e}_3 \tag{16}$$
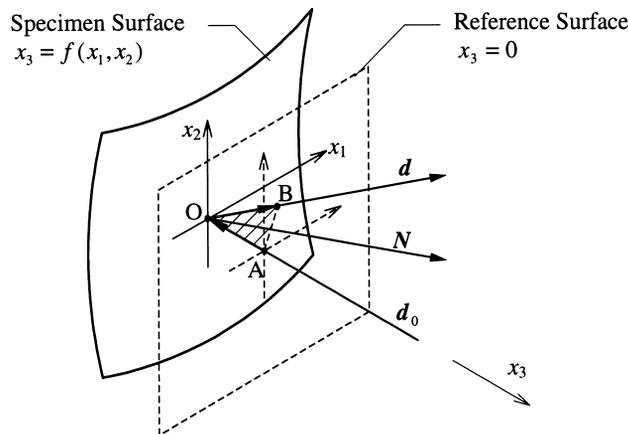
Substituting Eq. (11) into Eq. (16) yields

Fig. 3. Reflection of incident wave front from curved specimen surface.

$$\mathbf{d} = \alpha\mathbf{e}_1 + \beta\mathbf{e}_2 + \gamma\mathbf{e}_3 = \frac{2(-f_{,1}\mathbf{e}_1 - f_{,2}\mathbf{e}_2 + \mathbf{e}_3)}{1 + f_{,1}^2 + f_{,2}^2} - \mathbf{e}_3 \tag{17}$$

Thus,

$$\alpha = \frac{-2f_{,1}}{1 + f_{,1}^2 + f_{,2}^2}, \quad \beta = \frac{-2f_{,2}}{1 + f_{,1}^2 + f_{,2}^2}, \quad \gamma = \frac{1 - f_{,1}^2 - f_{,2}^2}{1 + f_{,1}^2 + f_{,2}^2} \tag{18}$$

To determine the change in the optical path length due to reflection from the curved specimen surface, as compared to reflection from a flat reference surface, consider the plane containing the unit incident and reflected vectors at any generic point (x_1, x_2) as shown in Fig. 3. The net change in optical path length at point (x_1, x_2) is given as

$$S(x_1, x_2) = |\bar{\mathbf{A}}\mathbf{O}(x_1, x_2)| + |\bar{\mathbf{B}}\mathbf{O}(x_1, x_2)|$$

$$= \left(\frac{f(x_1, x_2)}{\mathbf{d}(x_1, x_2) \cdot \mathbf{e}_3}\right)\mathbf{d}(x_1, x_2) + |f(x_1, x_2)\mathbf{e}_3| \tag{19}$$

Thus,

$$S(x_1, x_2) = f(x_1, x_2)\left(\frac{2}{1 - f_{,1}^2 - f_{,2}^2}\right) \tag{20}$$

Assuming $|\nabla^2 f| < 1$ and substituting Eq. (20) in Eq. (9) we get

$$\frac{\partial f(x_1, x_2)}{\partial x_\alpha} \approx \frac{n^{(\alpha)}p}{2\Delta}, \quad n^{(\alpha)} = 0, \pm 1, \pm 2, \dots \tag{21}$$

where $\alpha \in \{1, 2\}$. Eq. (21) are the basic governing equations that relate CGS fringe contours to in-plane gradients of the specimen surface $x_3 = f(x_1, x_2)$.

Now, in order to relate CGS interferograms of a given surface to its curvature consider a curved specimen as shown in Fig. 4a. The normal at a point, $P(\xi_1, \xi_2)$, on the surface is defined as,

$$\mathbf{a}_3 = \frac{\mathbf{a}_1 \times \mathbf{a}_2}{|\mathbf{a}_1 \times \mathbf{a}_2|} \tag{22}$$

where $\mathbf{a}_1$ and $\mathbf{a}_2$ are unit vectors tangent to the curvilinear coordinates axes (ξ_1, ξ_2). The unit tangent vectors, $\mathbf{a}_1$ and $\mathbf{a}_2$, are given in terms of the position vector, $\mathbf{r}(\xi_1, \xi_2, \xi_3)$, of the point $P(\xi_1, \xi_2)$ as $\mathbf{a}_\alpha = \partial r/\partial \xi_\alpha$, $\alpha \in \{1, 2\}$. The rate at which $\mathbf{a}_3$ varies between neighboring points provides a measure of curvature at the point of interest. Now,

$$d\mathbf{a}_3 = \frac{\partial \mathbf{a}_3}{\partial \xi_\alpha}d\xi_\alpha \tag{23}$$

Note that $\partial \mathbf{a}_3/\partial \xi_\alpha$ are tangent vectors since $\mathbf{a}_3 \cdot (\partial \mathbf{a}_3/\partial \xi_\alpha) = 0$. The curvature tensor κ is defined as the projections of the rate of change vectors $\partial \mathbf{a}_3/\partial \xi_\alpha$ along the unit tangent vectors $\mathbf{a}_3$ and $\mathbf{a}_2$ as

$$\kappa_{\alpha\beta} = -\frac{\partial \mathbf{a}_3}{\partial \xi_\alpha} \cdot \mathbf{a}_\beta, \quad \alpha, \beta \in \{1, 2\} \tag{24}$$

Or, in terms of the position vector $\mathbf{r}(\xi_1, \xi_2, \xi_3)$

$$\kappa_{\alpha\beta} = \mathbf{a}_3 \cdot \frac{\partial^2 \mathbf{r}}{\partial\xi_\alpha\partial\xi_\beta}, \quad \alpha,\beta \in \{1, 2\} \tag{25}$$

$\kappa_{\alpha\beta}$ is the symmetric curvature tensor whose components κ_{11} and κ_{22} are termed as the 'normal curvatures' and κ_{12} ($=\kappa_{21}$) as the 'twist'. The principal values of $\kappa_{\alpha\beta}$ are termed as the principal curvatures.

Consider the case of a shallow surface, $x_3 = f(x_1,x_2)$, as shown in Fig. 4b. The curvilinear coordinate systems reduces to

$$x_1 = \xi_1, \ x_2 = \xi_2, \ x_3 = \hat{f}(\xi_1,\xi_2) = f(x_1,x_2) \tag{26}$$

and

$$\mathbf{r}(x_1,x_2,x_3) + x_1, \mathbf{e}_1 + x_2\mathbf{e}_2 + f(x_1,x_2)\mathbf{e}_3 \tag{27}$$

Thus,

$$\kappa_{\alpha\beta} = \mathbf{a}_3 \cdot \frac{\partial^2 \mathbf{r}}{\partial x_\alpha\partial x_\beta} = \frac{f_{,\alpha\beta}}{\sqrt{1+f_{,1}^2+f_{,2}^2}}, \quad \alpha,\beta \in \{1, 2\} \tag{28}$$

For small curvatures, $|\nabla^2 f| < 1$ and thus,

$$\kappa_{\alpha\beta} \approx f_{,\alpha\beta}, \quad \alpha,\beta \in \{1, 2\} \tag{29}$$

Substituting Eq. (21) into Eq. (29), we get the basic equation that relate CGS fringes to specimen curvature,

$$\kappa_{\alpha\beta}(x_1,x_2) \approx \frac{\partial^2 f(x_1,x_2)}{\partial x_\alpha\partial x_\beta} \approx \frac{p}{2\Delta}\left(\frac{\partial n^{(\alpha)}(x_1,x_2)}{\partial x_\beta}\right),$$
$$n^{(\alpha)} = 0, \pm 1, \pm 2, \ldots \tag{30}$$

where $\alpha \in \{1, 2\}$. Eq. (30) is the principal governing equation for determining curvature tensor fields, $\kappa_{\alpha\beta}(x_1,x_2)$, ($\alpha,\beta \in \{1, 2\}$), from CGS interferograms. In this manner, CGS interferograms provide a full-field technique for determining the instantaneous value of the specimen curvature tensor at any point, (x_1,x_2).

3. Curvature measurement using high-resolution X-ray diffraction

This curvature measurement technique is based on the principle of diffraction of X-rays from single-crystal substrates [31]. The experimental setup is basically the X-ray rocking curve setup with a translation stage added to the rocking curve sample holder. Consider a monochromatic X-ray beam incident on a curved specimen at a point P. as shown in Fig. 5a. The specimen is typically a thin film coating supported on a single-crystal substrate. Now consider the diffraction of this incident X-ray beam from one of the crystallographic planes of the single-crystal substrate, and let these planes be oriented parallel to the specimen surface for the sake of illustration. The incident beam will be diffracted at an angle $2\theta^{(\alpha)}$, as governed by the Bragg law [30],

$$\sin\theta^{(\alpha)} = \frac{\lambda}{2d} \tag{31}$$

where λ is the X-ray wavelength, d the interplanar spacing of the crystallographic planes and $\alpha \in \{1, 2\}$ represents the fact that the angular change is in the (x_α,x_3) plane. Now consider a rigid body translation of the specimen along the x_α-direction, as shown in Fig. 5b. If the specimen surface was flat diffraction would occur as before and the diffraction peak would still be observed at the same location, D. However, since the specimen surface is curved the orientation of the currently diffracting crystallographic planes, which are parallel to the specimen surface, changes along with specimen translation. Thus, the angle of incidence of the X-ray beam has to be changed by an amount, $d\theta^{(\alpha)}$, to maintain Bragg angle diffraction, and the X-ray source moves from S to S'. Diffraction again occurs at the same angle $d\theta^{(\alpha)}$ as before, however the orientation of the diffracted beam also changes by $d\theta^{(\alpha)}$ and the X-ray detector location has to be changed from D to D'. The change in orientation of the diffracted (and incident) beams, $d\theta^{(\alpha)}$, is the same as the change in orientation of the currently diffracting crystallographic planes due to specimen curvature. For the case of small curvature, this change in the orientation is related to the specimen curvature as

$$\kappa_{\alpha\alpha} \approx \frac{d\theta^{(\alpha)}}{dx_\alpha}, \quad \alpha \in \{1, 2\} \ (\text{no sum}) \tag{32}$$

where dx_α is the translation distance along the x_α-direction.
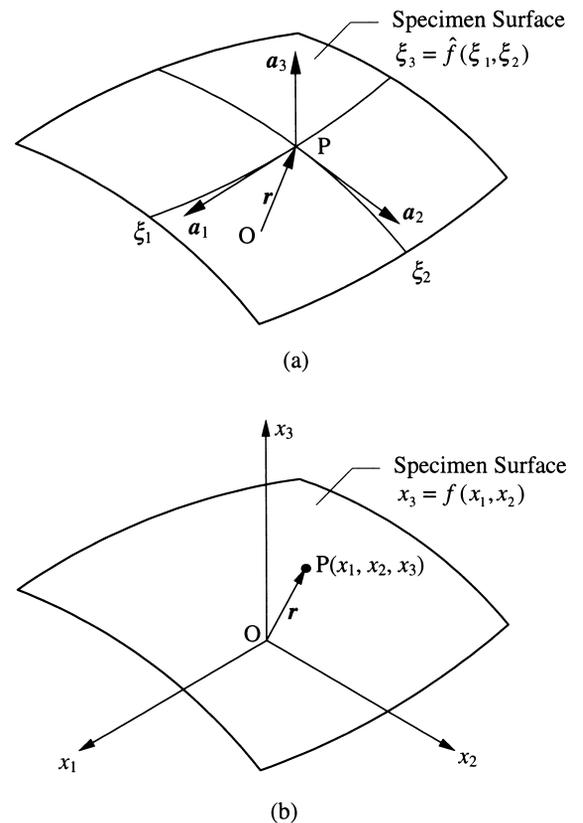

(a)

(b)

Fig. 4. (a) Curved specimen surface described in terms of curvilinear coordinates, and (b) shallow surface with small curvatures.

Note that the curvature is determined only in an averaged sense over the point of initial beam incidence, P, and point of beam incidence after translation, P′. Thus, gross non-uniformity in specimen curvature would lead to inaccurate measurements.

The major limitation to the high-resolution X-ray diffraction technique arises from the difficulty in translating the specimen without inducing any rigid body rotation. The translation stage usually induces a constant rigid body rotation for a given specimen translation. Thus, a translation of the curved specimen by a given distance dx_a results in an angular shift in the diffracted beam by an amount $d\omega^{(\alpha)} = d\theta^{(\alpha)} + d\phi^{(\alpha)}$, where $d\theta^{(\alpha)}$ is the contribution due to specimen curvature and $d\phi^{(\alpha)}$ is rotational error introduced

by the translation stage. The rotational error can be determined and corrected for by using a calibration procedure. This procedure involves the use of a nominally 'flat' specimen of the same crystallographic structure as the actual curved specimen whose curvature is being determined. Normally, this 'flat' specimen is part of the same single-crystal wafer that has been coated to form the thin film structure. The calibration specimen is placed in the X-ray diffraction setup and the location of the diffraction peak is noted. A translation of this specimen would 'ideally' result in no change in the location of the diffracted beam. However, since the translation stage introduces an erroneous rotation the diffraction peak will shift by an amount $d\omega^{(\alpha)} = d\phi^{(\alpha)}$, which represents the translation introduced error. Thus, the
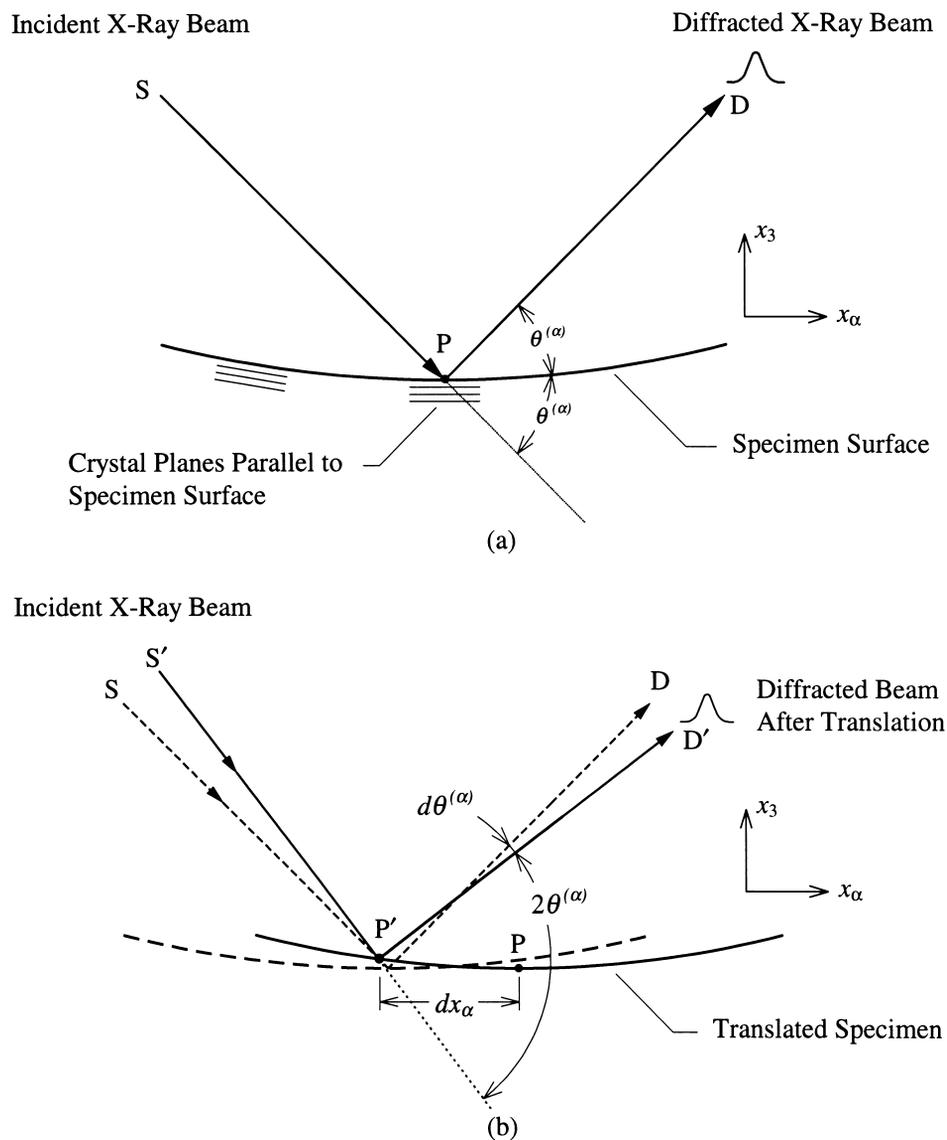

Fig. 5. Schematic to illustrate the working principle of high-resolution X-ray diffraction for curvature measurement: (a) diffraction from point P, and (b) diffraction from point P′ after specimen translation. S, D: X-ray source and detector locations; S′, D′: X-ray source and detector locations after specimen translation.
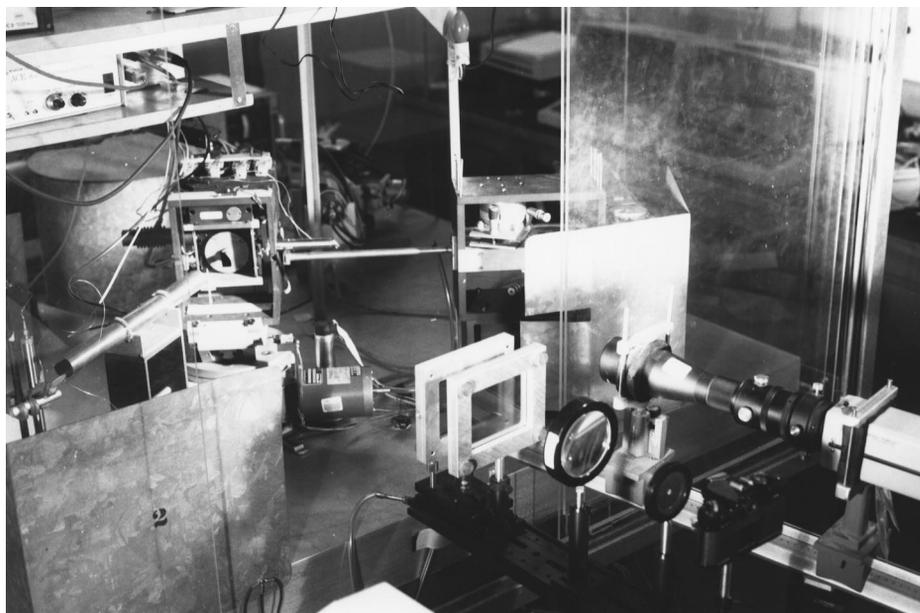
Fig. 6. Photograph showing the coherent gradient sensing interferometer and the high-resolution X-ray diffraction setup.

actual curvature of the specimen is determined by measuring its apparent curvature and correcting it by the apparent curvature of the reference calibration specimen, i.e.

$$\kappa_{\alpha\alpha} \approx \frac{d\theta^{(\alpha)}}{dx_\alpha} = \frac{d\omega^{(\alpha)}}{dx_\alpha} - \frac{d\phi^{(\alpha)}}{dx_\alpha}, \quad \alpha \in \{1, 2\} \text{ (no sum)} \quad (33)$$

where $d\omega^{(\alpha)}/dx_\alpha$ represents the apparent curvature of the specimen and $d\phi^{(\alpha)} = dx_\alpha$ the apparent curvature of the reference specimen. The net result of the calibration procedure is that the technique measures curvatures only relative to the reference specimen. Thus, the existence of a 'flat' reference specimen is a necessary requirement to ensure accuracy in interpreting the measurements as absolute curvatures.

4. Experimental setup, specimen geometry and results

The techniques of CGS and high-resolution X-ray diffraction were employed simultaneously to determine

Table 1

Layered structure of the multilayer-A and multilayer-B specimens obtained using Rutherford backscattering (RBS)

Layer constituent	Multilayer-A specimen	Multilayer-B specimen
TiN	–	50 nm
Al-x%Si	500 nm	500 nm
Ti	30 nm	30 nm
TiN	100 nm	100 nm
SiO$_2$	420 nm	420 nm
Si (substrate)	506 μm	506 μm

curvatures for two different specimens. A photograph of the experimental setup is shown in Fig. 6. Simultaneous measurements ensured that the curvatures determined by the two techniques could be compared without any ambiguity. The two specimens studied (designated as multilayer-A and multilayer-B) were manufactured by M.I.T.'s Lincoln Laboratories (Lexington, MA) and comprised multilayered thin films deposited on single-crystal silicon wafers. The layered structure of the two specimens obtained using Rutherford backscattering (RBS) is tabulated in Table 1.

CGS interferograms obtained for the multilayer-A specimen are shown in Fig. 7. Separate interferograms were obtained for wave front shearing in two orthogonal directions. These interferograms were then digitized and numerically differentiated to determine components of the curvature tensor field as per Eq. (30). These curvature components, κ_{11}, κ_{22} and κ_{12}, are plotted in Fig. 8. The specimen exhibited fairly uniform curvature towards the center despite considerable variation towards some of the edges. Also, there was about 18% difference in the normal curvatures, κ_1, and κ_{22}, measured along the x_1- and x_2-directions. This could be due to the inherent material anisotropy of the silicon substrate and the directional structural variation in the thin film coatings, associated with the fabrication process. The twist curvature, κ_{12}, was considerably smaller in magnitude than the normal curvatures, κ_{11} and κ_{22}, and had a maximum value near the specimen edge.

High-resolution X-ray diffraction was also used to determine curvature for the same specimen (multilayer-A). Angular profile of the diffracted beam obtained as the specimen was translated along the x_2-direction in uniform steps of 1 mm is plotted in Fig. 9. These peaks correspond to
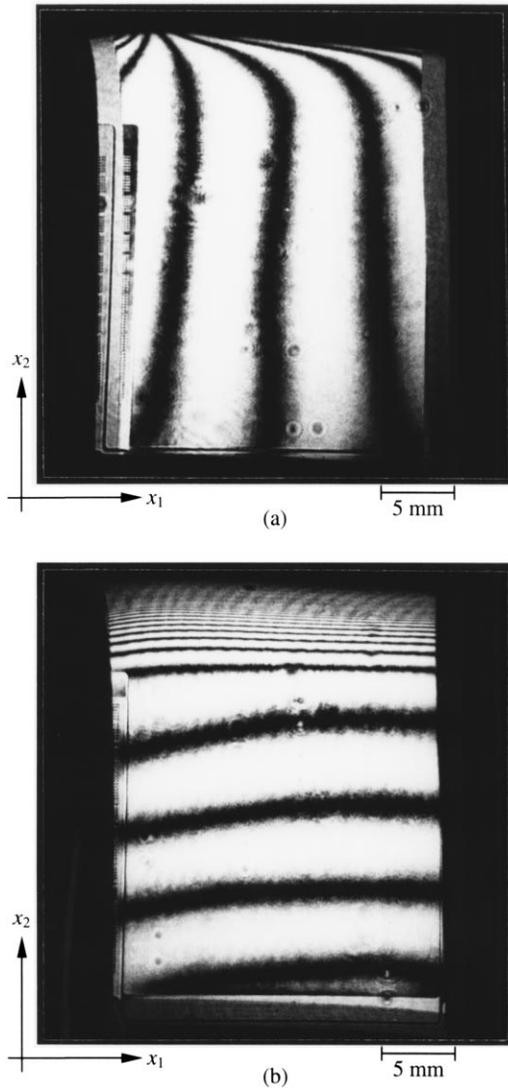
the x_2-direction. Curvature tensor components were determined as before, but are not presented here for the sake of brevity.

Since high-resolution X-ray diffraction measures curvature only in an averaged sense, the CGS data were also averaged to facilitate a direct comparison of curvatures obtained using the two techniques. Averaging of the curvature fields obtained using CGS was done in the center of the specimen, since this is the area where X-ray diffraction measures average curvature. Table 2 plots the averaged curvature measurement made using the two techniques for both multilayer-A and multilayer-B specimens. As given in Table 2, the agreement between the two techniques (for the κ_{22} component) was excellent. Note that direct comparison between the absolute curvatures measured by CGS and the relative curvatures measured by X-ray diffraction was possible in these cases because the reference specimen used to calibrate X-ray diffraction technique was 'extremely flat' ($\kappa < 0.002$ m^{-1}, as determined by CGS).

Fig. 7. CGS interferograms obtained for the multilayer-A specimen.

diffraction from the Si(100) crystallographic planes. These data were used to plot the angular orientation of the diffracted peaks as a function of specimen translation, as shown in Fig. 10. The data for the 'flat' reference specimen are also plotted in the same figure. The slope of the line fitted through the multilayer-A data represents the apparent specimen curvature, $d\omega^{(2)}/dx_\alpha$, while the slope of the line through the reference data represents $d\phi^{(2)}/dx_\alpha$. Thus, actual specimen curvature was obtained as a difference between the two slopes in accordance with Eq. (33), i.e. $\kappa_{22} = d\omega^{(2)}/dx_\alpha - d\phi^{(2)}/dx_\alpha = 0.050$ m^{-1}. X-Ray diffraction was used to measure curvature only along the x_2-direction since these measurements were made only for comparison with the CGS data.

CGS and high-resolution X-ray diffraction measurements were repeated for the multilayer-B specimen. As for the multilayer-A specimen, the CGS measurements were made along both the x_1- and x_2-directions while the X-ray diffraction measurements were made only along
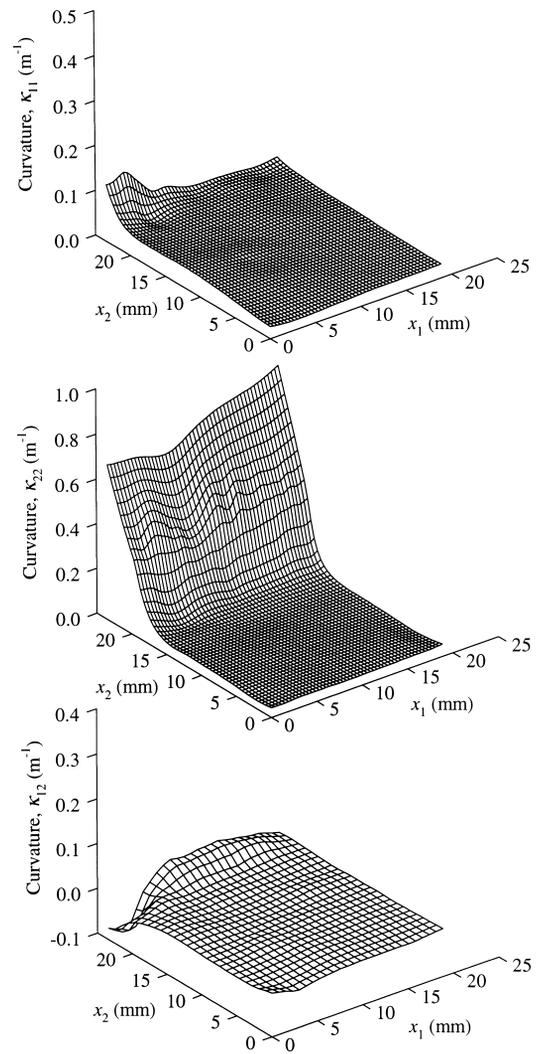

Fig. 8. Curvature tensor components, κ_{11}, κ_{22} and κ_{12}, obtained from CGS interferograms for multilayer-A specimen.
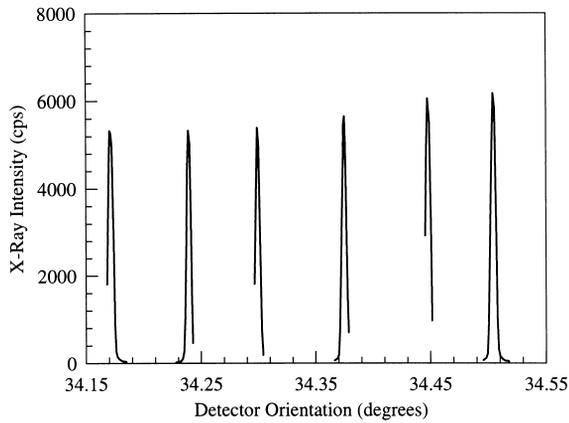
Fig. 9. Angular profile of the diffracted beam obtained as a function of specimen translation for multilayer-A specimen.
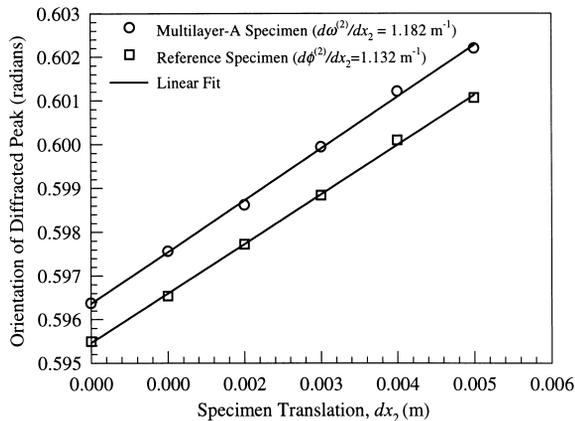

Fig. 10. Angular orientation of the diffracted peak as a function of specimen translation for the multilayer-A specimen and reference specimen.

5. Discussion

The full-field, optical technique of CGS has been established as a tool for measuring specimen curvature fields in thin film structures. The following examples are used to further demonstrate the application of CGS in measuring curvature fields in a wider variety of thin films and micromechanical structures.

As a first example, coherent gradient sensing interferometry was employed to determine the presence of a surface defect in a chromium-coated silicon wafer (320 nm Cr/324 μm Si). The CGS interferograms obtained for shearing in the two directions are shown in Fig. 11. These were analyzed in accordance with Eq. (30) to determine components of the curvature tensor field. It is apparent from the normal curvature components, κ_{11} and κ_{22}, shown in Fig. 12, that there is a highly localized region on the specimen that exhibits very high curvatures relative to the rest of the specimen. This region of high curvature represents a 'defect' in the form of a localized non-uniformity of the specimen surface. Whatever the cause of this surface non-uniformity, CGS interferometry is shown to be capable of identifying successfully such surface anomalies because of its full field nature. Other commonly used curvature measurement methods, such as high-resolution X-ray diffraction [30,31] or the laser scanning technique [32], provide point-wise information and could potentially miss such localized anomalies. Moreover, even if complete curvature maps are generated by scanning, these scans involve finite time and may not be adequate for time varying, non-uniform surface curvature fields (e.g. a growing delamination due to thermal cycling).

Table 2

Curvatures for multilayer-A and multilayer-B specimen obtained using CGS (averaged over specimen center) and high-resolution X-ray diffraction.

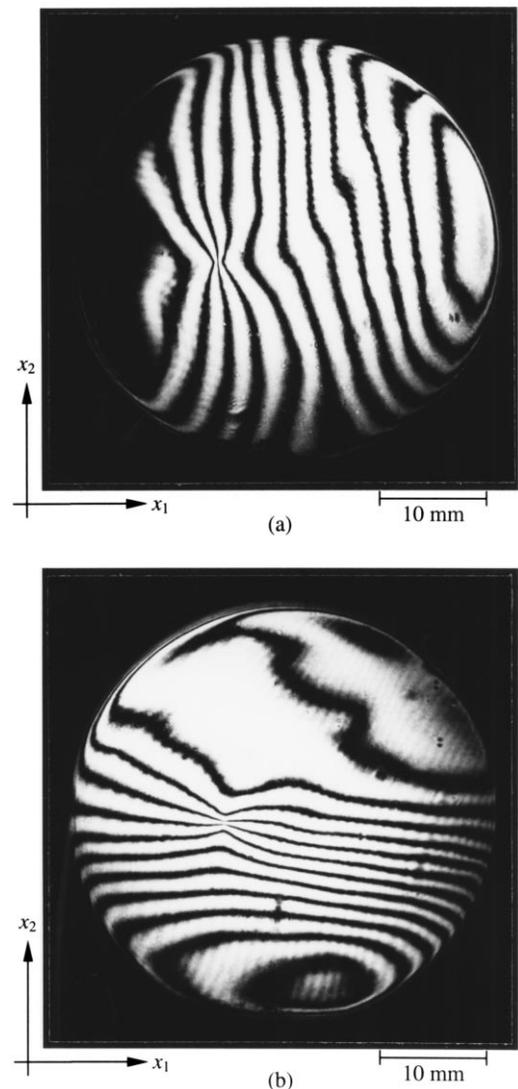| Curvature	Multilayer-A specimen		Multilayer-B specimen	
	CGS (m^{-1})	X-Ray diffraction (m^{-1})	CGS (m^{-1})	X-Ray diffraction (m^{-1})
κ_{11}	0.039	–	0.024	–
κ_{22}	0.048	0.050	0.039	0.042
$\kappa_{12}=\kappa_{21}$	−0.014	–	−0.004	–

Fig. 11. CGS interferograms obtained for a thin film chromium-coated silicon wafer with a localized surface defect.

On the other hand, CGS produces an instantaneous full-field map of the entire surface curvature fields.

CGS was also applied to determine curvature for a thin film aluminum-coated silicon wafer with patterned lines. This specimen was fabricated by deposition of a uniform Al-1%Si film (500 nm) on a silicon wafer (520 μm) using an rf magnetron. Subsequently, the aluminum coating was patterned to form lines with widths ranging from 10 to 100 μm using photolithography and etching. The CGS interferograms obtained for shearing in the two directions are shown in Fig. 13. As before, the interferograms were analyzed in accordance with Eq. (30) to determine components
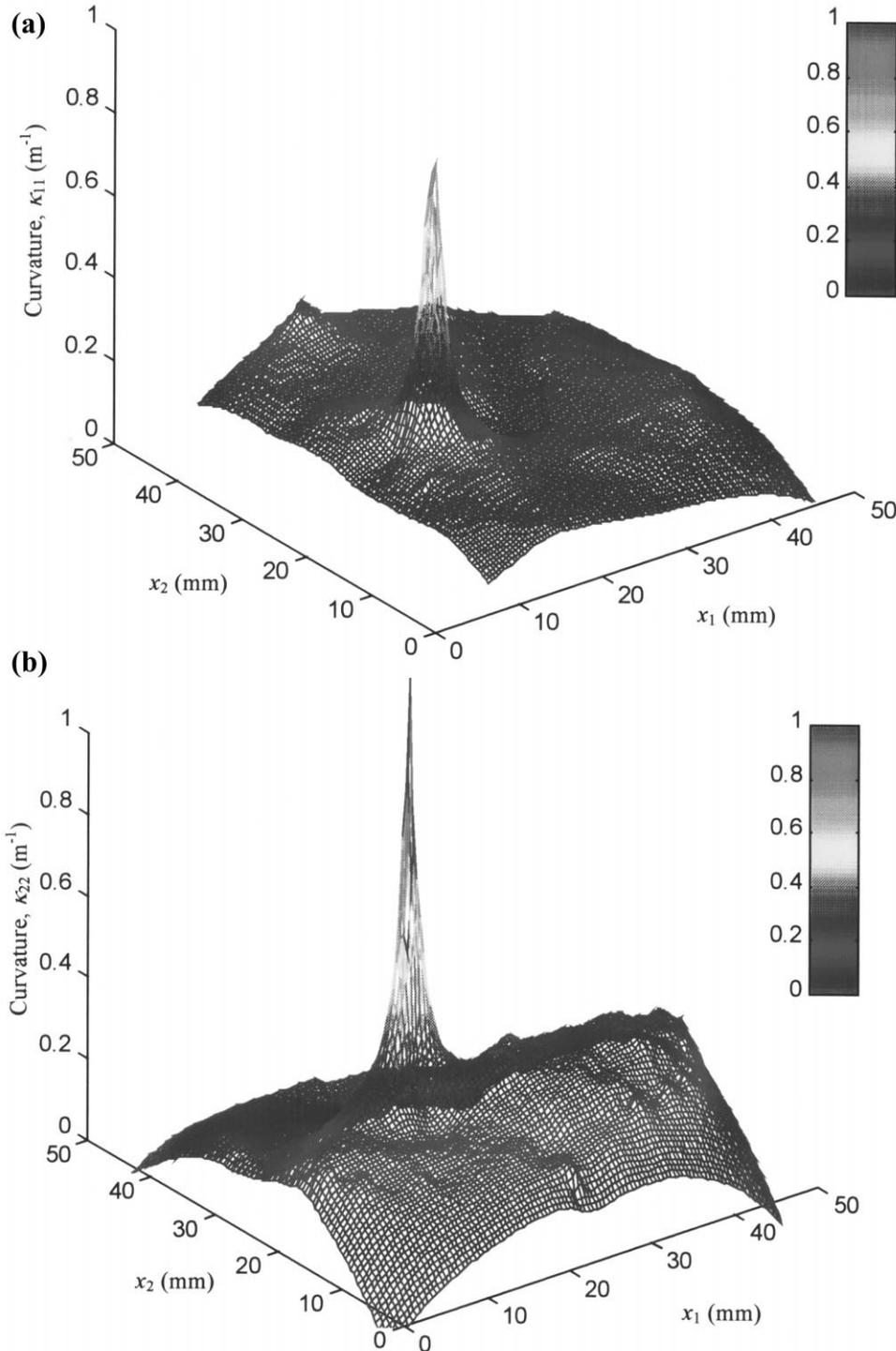
Fig. 12. (a) Normal curvature, κ_{22}, for a thin film chromium-coated silicon wafer with a localized surface defect as obtained from CGS interferograms. (b) Normal curvature, κ_{22}, for a thin film chromium-coated silicon wafer with a localized surface defect as obtained from CGS interferograms.
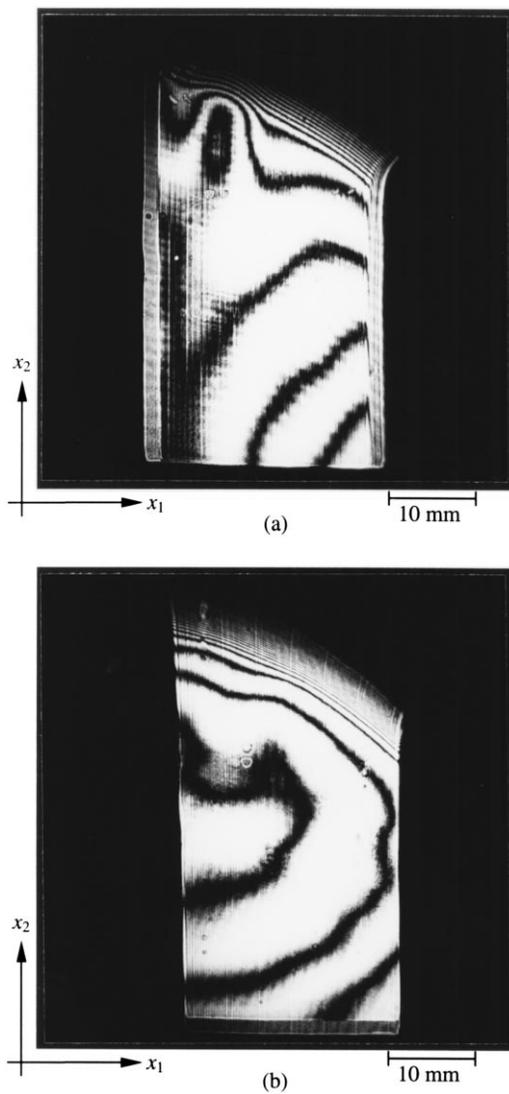
Fig. 13. CGS interferograms obtained for a thin film aluminum-coated silicon wafer with patterned lines.

of the curvature tensor field. The normal curvature field components, κ_{11} and κ_{22}, are plotted in Fig. 14. Figs. 13 and 14 clearly demonstrate that the technique of CGS is not limited to uniformly coated specimens and can indeed be applied to determine specimen curvatures even in the presence of patterned structures.

Transmission lines supported on micron-thin dielectric membranes are currently being used in the development of advanced microwave circuits. For example, the Wilkinson power-combiner shown in Fig. 15 was implemented using microstrip lines on a thin (1.4 μm) dielectric membrane [41]. The membrane is a trilayer of $SiO_2/Si_3N_4/SiO_2$ which is grown on a silicon wafer using thermal oxidation and low pressure chemical vapor deposition. Deposition conditions and layer thickness are controlled to minimize stresses (and curvatures) in the multilayer structure. The membrane is left free-standing by selective chemical etching of the silicon to open a window in the substrate beneath the conducting lines. The mechanical stability and low

stresses of the membrane structure are crucial for the performance and long-term reliability of the circuit. X-Ray diffraction techniques cannot be used to determine the stresses and/or curvatures in such membrane structures since the membranes themselves are amorphous and are not supported on any substrate (crystalline or amorphous). CGS was employed to determine curvature of the membrane structure and the interferogram obtained for shearing along the x_2-direction is shown in Fig. 16. As estimated from this interferogram the membrane structure was very 'flat' and had a normal curvature component of $\kappa_{22} < 0.015$ m^{-1}.

This paper presents the full-field, optical technique of CGS as a tool for measuring the instantaneous specimen curvature tensor fields in thin film and micromechanical structures. CGS offers several advantages inherent to all full field optical techniques. It provides real-time, remote, non-intrusive, full-field measurements of curvature. Moreover, since it provides out-of-plane gradients of the specimen surface topography, $x_3 = f(x_1,x_2)$, the technique is not sensitive to rigid body rotation or displacement of the specimen surface. Thus, unlike other interferometric techniques, such as Twyman–Green interferometry [37–39], CGS is relatively vibration-insensitive. In addition, since CGS measures gradients of surface topography, only one differentiation operation of the experimental data is required to obtain
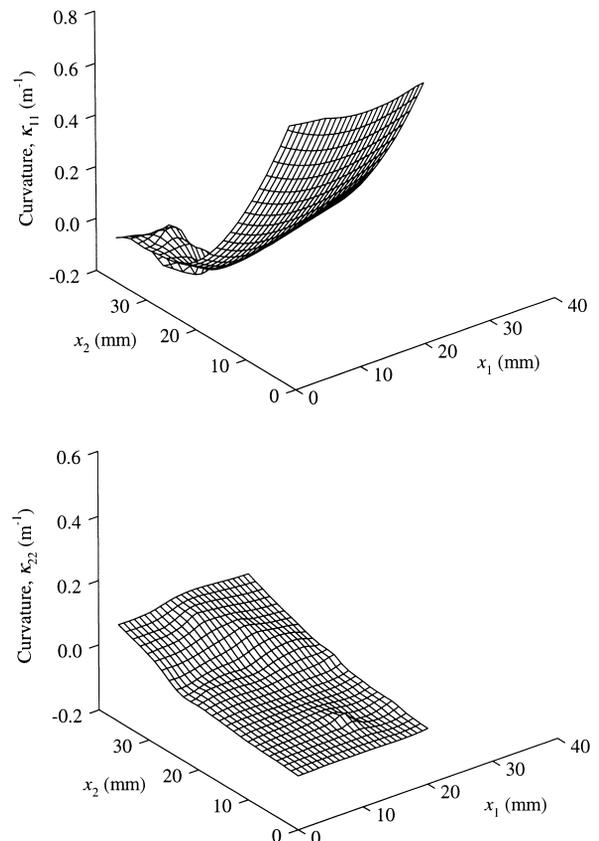

Fig. 14. Specimen curvatures obtained from CGS interferograms for a thin film aluminum-coated silicon wafer with patterned lines.
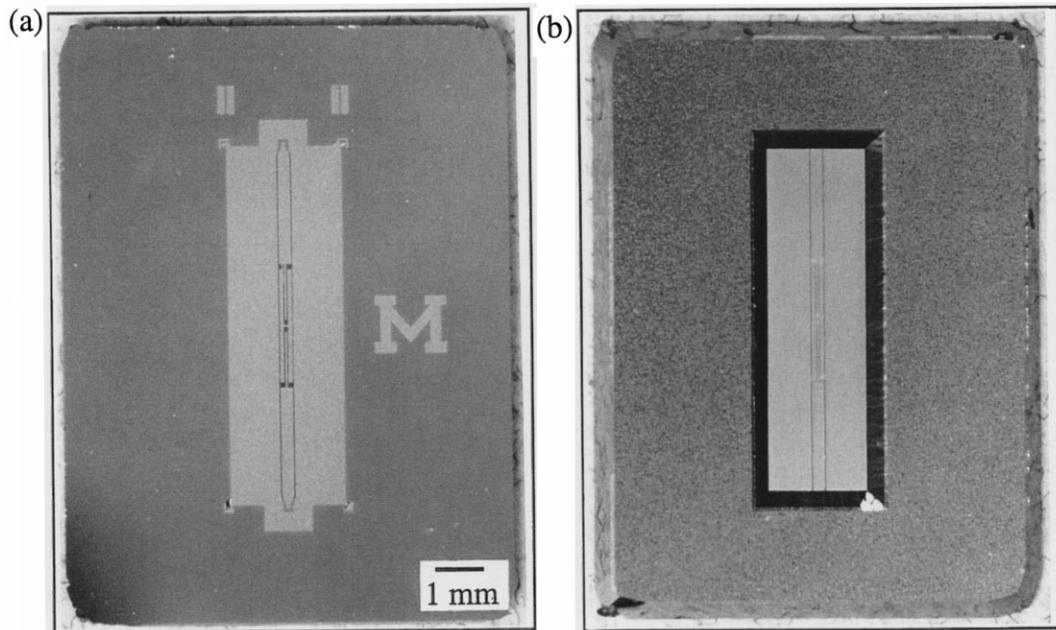
Fig. 15. Photograph of the membrane structure: (a) top view showing the Wilkinson power-combiner supported on a $SiO_2Si_3N_4/SiO_2$ membrane, and (b) bottom view showing the silicon substrate with etched window.

curvature. This is unlike other interferometric techniques, such as Twyman–Green interferometry [37–39], where curvature calculations will involve two successive differentiation operations. Finally, the application of CGS requires only a specularly reflective surface. Unlike X-ray diffraction methods that require the substrate to be a single crystal, CGS is not restricted by the form of the substrate.
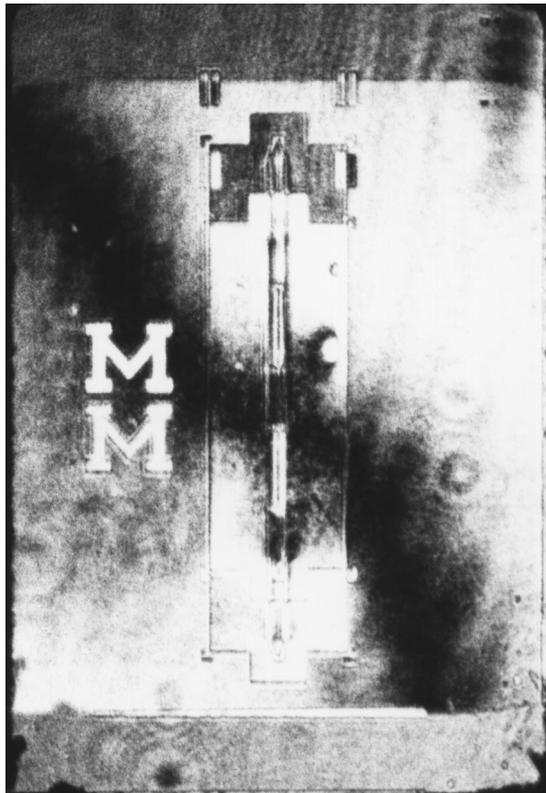
Fig. 16. CGS interferogram obtained for the membrane structure. (Shearing along the x_2-direction.)

References

[1] The National Technology Roadmap for Semiconductors, Semiconductor Industry Association, 1994.
[2] T. Seidel, B. Zhao, Mater. Res. Soc. Proc. 427 (1996) 3.
[3] W.D. Nix, Metall. Trans. 20A (1989) 2217.
[4] C.-Y. Li, P. Totta, P. Ho (eds.), Stress Induced Phenomena in Metallization: First International Workshop, AIP Conference Proceedings, 1992, p. 263.
[5] P.S. Ho, C.-Y. Li, P. Totta, (eds.), Stress Induced Phenomena in Metallization, AIP Conference Proceedings, 1993, p. 305.
[6] F.M. d'Heurle, Int. Mater. Rev. 34 (1989) 53.
[7] J. Klema, R. Pyle, E. Domangue, Proc. 22nd Annual EEE Int. Reliability Physics Symp., 1984, p. 1.

[8] K. Tokunaga, K. Sugawara, J. Electrochem. Soc. 138 (1) (1991) 176.

[9] J.W. McPherson, C.F. Dunn, J. Vac. Sci. Technol. B5 (5) (1987) 1321.

[10] F.G. Yost, Scripta Metall. 23 (1989) 1323.

[11] A.I. Sauter, W.D. Nix, Mater. Res. Soc. Proc. 188 (1990) 153.

[12] C.A. Paszkiet, M.A. Korhonen, C.-Y. Li, Mater. Res. Soc. Proc. 203 (1990) 381.

[13] J.G. Ryan, J.B. Riendeau, S.E. Shore, G.J. Slusser, D.C. Beyar, D.P. Bouldin, T.D. Sullivan, J. Vac. Sci. Technol. B9 (1990) 1474.

[14] S. Mayumi, T. Umemoto, M. Shishino, H. Nanatsue, S. Ueda, M. Inoue, Proc. 25th Annual EEE Int. Reliability Physics Symp., 1987, p. 15.

[15] A. Tanikawa, H. Okabayashi, Proc. 28th Annual EEE Int. Reliability Physics Symp., 1990, p. 194.

[16] A. Tezaki, T. Mineta, H. Egawa, Proc. 28th Annual IEEE Int. Reliability Physics Symp., 1990, p. 221.

[17] M.A. Moske, P.S. Ho, C.K. Hu, M.B. Small, Proc. 1st Int. Workshop on Stress Induced Phenomena in Metallization, Ithaca, NY, 1992, p. 195.

[18] P. Borgesen, M.A. Korhonen, D.D. Brown, C.-Y. Li, Proc. 1st Int. Workshop on Stress Induced Phenomena in Metallization, Ithaca, NY, 1992, p. 219.

[19] J.E. Sanchez, Jr., O. Kraft, E. Arzt, Proc. 1st Int. Workshop on Stress Induced Phenomena in Metallization, Ithaca, NY, 1992, p. 251.

[20] M.A. Korhonen, P. Borgese, C.-Y. Li, Proc. 1st Int. Workshop on Stress Induced Phenomena in Metallization, Ithaca, NY, 1992, p. 29.

[21] T.D. Sulliva, L. Miller, G. Endicott, Proc. 1st Int. Workshop on Stress Induced Phenomena in Metallization, Ithaca, NY, 1992, p. 136.

[22] I.A. Blech, IEEE Int. Reliability Physics Symp. Tutorials, 1986.

[23] P.B. Guste, Solid State Technol. 20 (1983) 113.

[24] P.S. Ho, T. Kwok, Rep. Prog. Phys. 52 (1989) 301.

[25] H.H. Hoang, J.M. McDavid, Solid State Technol. 11 (1988) 5.

[26] G. Vaidya, D.B. Fraser, W.S. Lindenberger, J. Appl. Phys. 51 (1980) 4475.

[27] J.R. Lloyd, P.M. Smith, G.S. Prokop, Thin Solid Films 93 (1982) 385.

[28] D.S. Gardner, J.D. Meindl, K.C. Saraswat, EEE Trans. Electron. Devices 34 (3) (1987) 633.

[29] K.A. Danso, L. Tullos, Microelectron. Reliab. 21 (1981) 513.

[30] B.D. Cullity, Elements of X-ray Diffraction, Addison-Wesley, Reading, MA, 1978.

[31] T. Vreeland, A. Dommann, C.-J. Tsai, M.-A. Nicolet, Mater. Res. Soc. Proc. 30 (1988) 3.

[32] P.A. Flinn, D.S. Gardner, W.D. Nix, EEE Trans. Electron. Devices 34 (1987) 689.

[33] G.G. Stoney, Proc. R. Soc. Lond. A 82 (1909) 172.

[34] M. Finot, S. Suresh, J. Mech. Phys. Solids 44 (5) (1996) 683.

[35] L.B. Freund, J. Cryst. Growth 132 (1993) 341.

[36] L.B. Freund, J. Mech. Phys. Solids 44 (5) (1996) 723.

[37] M. Born, E. Wolf, Principles of Optics, Pergamon Press, New York, 1986.

[38] S. Park, M.S. Dadkhah, E. Motamedi, Abstract Proc. VIIth Int. Congr. on Experimental Mechanics and Experimental/Numerical Mechanics in Electronic Packaging, 1996, p. 7.

[39] B. Han, Y. Guo, Experimental/Numerical Mechanics in Electronic Packaging, 1(1), 1996, pp. 1–14.

[40] Y.J. Lee, J. Lambros, A.J. Rosakis, Optics Lasers Eng. 25 (1) (1996) 25.

[41] T.M. Weller, L.P. Katehi, M.I. Herman, P.D. Wamhof, EEE Trans. Microwave Theory Tech. 2 (1994) 911.